

Thermally activated leakage current in high-performance short-wavelength quantum cascade lasers

Y. V. Flores, M. P. Semtsiv, M. Elagin, G. Monastyrskyi, S. Kurlov, A. Aleksandrova, J. Kischkat, and W. T. Masselink

Department of Physics, Humboldt University Berlin, Newtonstrasse 15, D-12489 Berlin, Germany

(Received 8 January 2013; accepted 12 March 2013; published online 3 April 2013)

The threshold condition for a 4-level quantum cascade laser (QCL)-active region is formulated to include thermally activated leakage of charge carriers from active region confined states into states with higher energy. A method is described and demonstrated to extract the associated thermal escape current density from measurements at laser threshold. This current is modeled by including both the temperature dependent subband-distribution of charge carriers and longitudinal optical-phonon probability. The method is used to analyze the thermally activated leakage of charge carriers in two short-wavelength strain-compensated InGaAs/InAlAs QCL-structures. The energies of the higher-lying states extracted from the model are in good agreement with the values calculated numerically within the effective-mass approximation. The estimated scattering time for the thermal activation process agrees with the expected value as well. Our approach offers a straightforward and accurate method to analyze and troubleshoot thermally activated leakage in new QCL-active region designs. © 2013 American Institute of Physics.

[<http://dx.doi.org/10.1063/1.4798358>]

I. INTRODUCTION

Since their invention, quantum cascade lasers¹ (QCLs) have been rapidly developed into an important class of lasers that cover a wide wavelength range (3–300 μm). Because of their unipolar operation, active regions can be cascaded, allowing high output power even at long wavelengths. Furthermore, because of the parallel dispersion of the subbands, the gain spectrum of QCLs is narrow compared to the gain spectrum associated with interband transitions in semiconductor laser diodes. QCLs are the light sources of choice for a variety of applications including optical spectroscopy, gas sensing for both medical and environmental applications, and infrared (IR) countermeasures.^{2–4} For all of these applications, QCLs emitting in the two atmospheric windows, 3–5 and 8–13 μm , are of special interest.

An important aspect of QCL performance is its dependence on temperature. High average power or continuous-wave (cw) operation depends not only on extracting heat from the active region but also on designing the laser to be relatively insensitive to the increased temperature of the active region. Nevertheless, the mechanisms through which the active region temperature affects the QCL characteristics are not thoroughly researched. A better understanding of the several non-radiative scattering mechanisms involved in carrier's transport in QCLs is needed to design new structures and optimize their performance. The mainly non-radiative intersubband scattering channel in QCLs can be taken to be mediated through an electron-longitudinal optical (LO)-phonon interaction, allowing scattering with little change in energy between different electron subbands but with different values of crystal momentum. This process is especially acute for devices operating in the mid-IR where $\hbar\omega \gg E_{LO}$.^{5,6} On the other hand, electron-electron interaction processes represent the dominant contribution to intrasubband scattering,

with scattering rates at least two orders of magnitude larger than intersubband scattering rates, justifying the assumption of thermalized electron subbands.⁷

As pointed out by several authors,^{3,6,8,9} a particular electron-(LO) phonon interaction process with direct consequences in QCLs performance is the thermal activation of charge carriers from active region quantum well (QW) confined states into higher levels. As a consequence, the effective lifetime of the upper laser level is reduced and the injected current necessary to achieve laser action is increased. Sirtori and Teissier³ described this thermal escape current making the analogy to the model for calculating dark current in quantum well infrared photodetectors. As a result, they described this current to be $J_{esc} = C \cdot \exp(-E_{ij}/k_B T_e)$. Here, $E_{ij} = E_j - E_i$ is the escape barrier height or activation energy, assumed to be the energy difference between the two levels involved, k_B is the Boltzmann-constant, and T_e is the electronic temperature in the initial subband. The scattering time included in the constant C was estimated to be $t_{scatt} \approx 0.2 \text{ ps}$ for LO-phonon absorption.³

Pflügl *et al.*⁸ used a more general form of this expression, allowing a temperature dependence of the scattering rate: $C \rightarrow C(T)$. Fitting experimental data from current-voltage measurements on InGaAs/InAlAs QCLs with this approach, and assuming the subband dynamics of charge carriers to be determined by the lattice temperature, the expected activation energies were obtained. The temperature dependence of $C(T)$, however, remained difficult to describe.

Furthermore, since the thermal activation of charge carriers in QCL structures is given by a LO-phonon absorption mechanism, the escape barrier height is expected to be reduced by the LO-phonon energy.^{6,9} The phonon absorption process, on the other hand, depends on the phonon occupation probability in the material, analogous to the description of Botez *et al.*⁶

In this paper, we formulate an accurate and straightforward extension of the 3-level threshold condition for QCLs¹⁻³ to include thermally activated leakage of charge carriers from active region confined states into higher states (4-level active region). We further propose a method to determine the current component arising for thermal activation at laser threshold. This current is modeled taking both the temperature dependent subband-distribution of charge carriers and LO-phonon probability. As a result, a generalization of the expression given by Sirtori and Teissier³ is obtained, including a temperature dependence of the prefactor $C(T)$. The method is based on analyzing the temperature and $1/L$ -dependence of the threshold current density to obtain the gain as a function of temperature. Then, by considering that the leakage current vanishes at low temperatures and that the waveguide loss is due to free-carrier absorption, the leakage current is extracted as a function of temperature. This method is then used to analyze and compare the thermally activated leakage of charge carriers in two short wavelength strain-compensated InGaAs/InAlAs QCL-structures.

II. QCL THRESHOLD CONDITION UNDER THERMAL ACTIVATION

Figure 1 shows a reduced 4-level QCL active region. Electrons coming from the high electron concentrated injector ground state are injected either into the upper laser level 3, with an efficiency η_{inj} , or scattered into a higher state absorbing a LO-phonon, with an efficiency $(1 - \eta_{inj})$. The injected carriers into state 3 may scatter forward into a higher state absorbing a LO-phonon, scatter radiatively into the lower laser state 2, or follow other non-radiative scattering paths (Figure 1). The final state for thermally activated charge carriers is denoted in the following as state 4. A natural candidate for this state is the next confined level with higher energy than the initial state. However, in general terms, besides the condition between the subbands-minima $E_4 > E_{inj} + E_{LO}$ for scattering from the injector, and $E_4 > E_3 + E_{LO}$ for scattering from the upper laser state, the state 4 would be the state with the highest scattering probability for LO-phonon absorption.

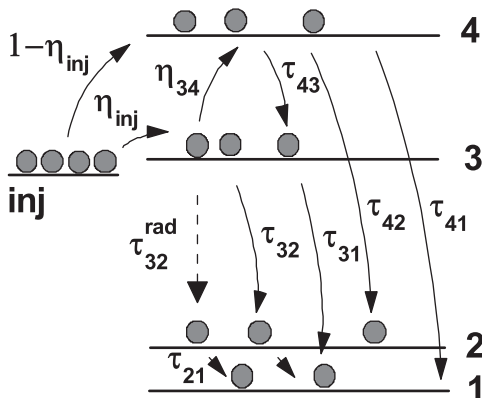


FIG. 1. Schematic representation of a 4-level QCL-active region. Black arrows show relevant non-radiative scattering paths and injection efficiencies. The dashed arrow represents the lasing transition.

In this simplified model, the rate equation for the upper laser state reads

$$\frac{dn_3}{dt} = \frac{\eta_{inj}(1 - \eta_{34})J}{e} + \frac{n_4}{\tau_{43}} - \frac{n_3}{\tau_3}, \quad (1)$$

where $\tau_3^{-1} = (\tau_{32}^{rad})^{-1} + \sum_{i \neq 3,4} \tau_{3i}^{-1}$ is the sum of radiative and non-radiative scattering rates. Similar expressions are obtained for levels 2 and 4. Note that the portion of thermally activated charge carriers from the upper laser state $n_3/\tau_{34} = \eta_{inj}\eta_{34}(J/e)$ is written in terms of a current density, the thermal escape current density for charge carriers scattered from state 3 to state 4. Direct injection of charge carriers from the injector ground state into lower laser levels is neglected within this approach due to the reduced space overlap between these levels in 3 QW structures, as illustrated by Faist *et al.*¹⁰ This assumption is supported, on the other hand, by the relatively high energy separation between injector and lower laser states in short-wavelength QCLs, and the consequent reduction of the non-radiative scattering via LO-phonon emission.

Rewriting the rate equations at equilibrium, the total sheet densities can be written

$$n_2 = n_3\tau_2[\tau_{32}^{-1} + (\tau_{32}^{rad})^{-1}] + n_4\frac{\tau_2}{\tau_{42}}, \quad (2a)$$

$$n_3 = \frac{\eta_{inj}(1 - \eta_{34})J}{e}\tau_3 + n_4\frac{\tau_3}{\tau_{43}}, \quad (2b)$$

$$n_4 = \frac{[1 - \eta_{inj}(1 - \eta_{34})]J}{e}\tau_4. \quad (2c)$$

The difference between the current density $\eta_{inj}J$ injected into the upper laser level and the escape current $\eta_{inj}\eta_{34}J$ from the upper laser state can then be thought in this simplified model as an “effective” current density populating the upper laser level $\eta_{inj}(1 - \eta_{34})J = \eta_3J$. Similarly, the total current density for electrons populating state 4 is given by

$$[1 - \eta_{inj}(1 - \eta_{34})]J = \eta_{esc}J = J_{esc}, \quad (3)$$

the (total) thermal escape current density. η_{esc} is then the total efficiency for thermal activation of charge carriers from both the injector ground state and the upper laser level.

In order to avoid unnecessarily long expressions, we shall take $\tau_{32}^{rad} \gg \tau_{32}$, as typically concluded from radiative life time calculations.¹¹ The relative values of τ_{32}^{rad} and the non-radiative lifetimes τ_{31} and τ_{32} , however, do not affect the analysis of the leakage current.

The laser gain $G = \Gamma\sigma(n_3 - n_2)$ is proportional to the difference in charge carrier’s concentrations in the upper- and lower laser levels, with $\sigma = \frac{4\pi e^2 \langle z_{32} \rangle^2}{\lambda \epsilon_0 n_{eff} (2\gamma_{32}) L_p}$ the stimulated emission cross-section of the radiative transition.^{2,3} Here, Γ is the mode overlap within the active region or confinement factor, e is the elementary charge, $\langle z_{32} \rangle$ is the dipole matrix element for the radiative transition, λ is the central emission wavelength, ϵ_0 is the vacuum permittivity, n_{eff} is the structure’s effective refractive index, $(2\gamma_{32})$ is the full width at half maximum of the luminescence spectrum, and L_p is the

structure's period length. Using Eqs. (2a) and (2b), a linear dependence of the laser gain $G = \eta_3 J g \Gamma$ on the injected current density J is found. The modal gain coefficient $g \Gamma$ gives then the gain per current density injected "effectively" into the upper laser level and is written as

$$g \Gamma = \frac{\sigma \Gamma}{e} \left\{ \tau_3 \left(1 - \frac{\tau_2}{\tau_{32}} \right) - \frac{\eta_{esc}}{\eta_3} \tau_4 \left(\frac{\tau_2}{\tau_{42}} - \frac{\tau_3}{\tau_{43}} \left[1 - \frac{\tau_2}{\tau_{32}} \right] \right) \right\}. \quad (4)$$

This expression represents a small correction of the order of η_{esc}/η_3 to the "effective" upper laser level lifetime $\tau_{up} = \tau_3(1 - \tau_2/\tau_{32})$ in the 3-level approximation ($\eta_{esc} = 0$).^{2,12}

At threshold, the current density can be written

$$J_{th} = J_{th}^0 + J_{th}^{esc} = (\alpha_m + \alpha_w)/(g \Gamma) + J_{th}^{esc}, \quad (5)$$

where J_{th}^0 is the threshold current density without leakage determined by the gain and losses and J_{th}^{esc} is the current that is lost as charge carriers scatter into level 4. The mirror and waveguide losses are given by α_m and α_w .

III. MODELING THE THERMAL ESCAPE CURRENT DENSITY

Consider charge carriers within a subband i with sufficient energy to scatter into a higher energy state j while absorbing a LO-phonon. If the charge carrier's energy lies within an infinitesimal interval $[E, E + dE]$, the correspondent differential current density can be written as

$$dJ_{ij}(E, T_l, T_{e,i}) = \frac{e}{\tau_{ij}(E, T_l)} D^{2D} f_e^{FD}(E, T_{e,i}), \quad (6)$$

where e is the elementary charge, $1/\tau_{ij}(E, T_l)$ is the energy- and (lattice) temperature-dependent LO-phonon absorption scattering rate, D^{2D} is the (constant) two-dimensional density of states, and $f_e^{FD}(E, T_{e,i}) = [\exp((E - E_{F,i})/k_B T_{e,i}) + 1]^{-1}$ is the Fermi-Dirac distribution function for electrons in state i , defined in terms of the subband's electronic temperature $T_{e,i}$. The subband's quasi-Fermi energy $E_{F,i}$ is defined in

$$n_i = \int_{E_i}^{\infty} D^{2D} f_e^{FD}(E, T_{e,i}) dE, \quad (7)$$

where n_i is the total charge carrier's density in the i th-subband and E_i is the subband's minima.

Typical two dimensional carrier concentrations in QCL-structures lie in the $n_i \sim 10^{10} \text{ cm}^{-2}$ order of magnitude.^{13,14} At this limit, the quasi Fermi-Level $E_{F,i}$ lies several tens of millielectron volts below the subband's minima E_i . Thus, since for the following analysis only the distribution's tail is relevant, we write the electron's distribution function assuming Maxwell-Boltzmann statistics $f_e^{MB}(E, T_{e,i}) = \exp[(E_{F,i} - E)/k_B T_{e,i}]$.

On the other hand, the temperature dependence of the scattering rate $1/\tau_{ij}(E, T_l)$ is principally controlled by the phonon density in the material,¹⁴⁻¹⁷ which can be written using Bose-Einstein statistics as $n_{LO}(T_l) = [\exp(E_{LO}/k_B T_l) - 1]^{-1}$. In the temperature range of 100–300 K, and for typical phonon

energies $E_{LO} \sim 30 \text{ meV}$, this dependence can be well approximated by a Maxwell-Boltzmann distribution function $f_{ph}^{MB}(E_{LO}, T_l) = \exp(-E_{LO}/k_B T_l)$. This approximation allows a simple and compact final result, while maintaining sufficient accuracy to allow useful conclusions to be drawn. Doing this, the scattering rate is written as a product of a temperature dependent Boltzmann-factor and a nearly temperature-independent part

$$\tau_{ij}(E, T_l)^{-1} \approx f_{ph}^{MB}(E_{LO}, T_l)/\tau_{ij}(E). \quad (8)$$

The total escape current density results from integrating $dJ_{ij}(E)$ as

$$J_{ij} = e \left[\int_{E_j - E_{LO}}^{\infty} \frac{D^{2D}}{\tau_{ij}(E)} \exp\left(\frac{E_{F,i} - E}{k_B T_{e,i}}\right) dE \right] \exp\left(\frac{-E_{LO}}{k_B T_l}\right). \quad (9)$$

A straightforward evaluation of the integral in square brackets in Eq. (9) would require an extended analysis of the term $\tau_{ij}(E)$. Furthermore, a weighting method of $\tau_{ij}(E)$ over the energy scale has been proposed in Harrison's book¹⁴ within the effective mass approximation, resulting in an expression that requires numerical evaluation in order to get tangible results. In this paper, however, an *averaged* value for this term $\tau_{ij}(E) \rightarrow \tau_{esc}$ over the energy scale is considered and factored out of the integral in Eq. (9), allowing the formulation of an elegant and compact expression for the escape current density. A similar step has been used by Liu *et al.*¹⁸ while deriving their formula for dark current in quantum well infrared photodetectors. As a result, the remaining integral in Eq. (9) represents the total two-dimensional electron concentration in subband i with sufficient energy to reach state j with help of a LO-phonon.

Combining Eqs. (7) and (9), and reintroducing the notations of Sec. II, we obtain

$$J_{esc} = \frac{en_i}{\tau_{esc}} \exp\left[-\frac{E_{esc} - E_{LO}(1 - T_{e,i}/T_l)}{k_B T_{e,i}}\right], \quad (10)$$

where the index $i = \{3, inj\}$ is related either to the upper laser state or to the injector ground state and $E_{esc} = E_4 - E_i$ is the energy difference between the initial state i and state 4, or activation energy. Note that the exponential factor agrees with the LO-phonon absorption scattering rates estimated by Botez *et al.*^{6,19} For equal electronic and lattice temperatures ($T_{e,i} = T_l$), the factor multiplying the phonon energy E_{LO} vanishes, and Eq. (10) reduces to the expression given by Sirtori and Teissier.³ Furthermore, as already mentioned, Sirtori and Teissier indicate that the derivation of their formula is identical to the illustrated in publication of Liu *et al.*¹⁸ This agreement is, however, a coincidence since if integrating Eq. (9) from E_j instead of $E_j - E_{LO}$, and leaving out the Boltzmann factor, the same result as in Sirtori and Teissier³ is obtained.

IV. THERMALLY ACTIVATED LEAKAGE IN TWO SHORT-WAVELENGTH QCL-STRUCTURES

Here, the investigated QCL-designs are presented (Sec. IV A). A method to extract the escape current density

based on measurements at laser threshold is described and applied on both structures (Sec. IV B). The extracted escape current densities are then modeled and the activation energies and scattering times for the thermal escape process are determined (Sec. IV C). Results are discussed in Sec. IV D.

A. Investigated QCL-structures

The investigated QCL-designs (structures S1 and S2) are devices emitting in the mid-IR range. The active region of the first design, referred in the following as structure S1, has been designed following an innovative concept aimed to manage the interface-scattering rate.^{20,21} This results in an increased upper laser state's lifetime while the lower laser state's lifetime is decreased, favoring population inversion. A portion of the conduction band profile of structure S1 is shown in Figure 2. The effective-mass approximation is included into calculations, as well as non-parabolicity effects and strain induced energy shifts. Layers composition and thickness are indicated in the original publication by Semtsiv *et al.*²⁰ In order to reduce the thermal escape current, large energy separations between the upper laser level and higher states are achieved in this structure. As Table I indicates, energy separations $E_{34} = 118$ meV and $E_{35} = 176$ meV between subband's minima are calculated for structure S1.

Structure S2 (Fig. 3) is similar to the previous one, though especially designed to enhance the thermal escape current by means of a reduced activation energy E_{esc} (Eq. (10)). For this purpose, energy separations $E_{34} = 81$ meV and $E_{35} = 139$ meV are achieved in structure S2, representing reduced values relative to structure S1. Furthermore, other leakage mechanisms are simultaneously increased in structure S2. The direct injection of charge carriers from the injector ground state into lower laser states via LO-phonon emission, for example, will be in the longer-wavelength

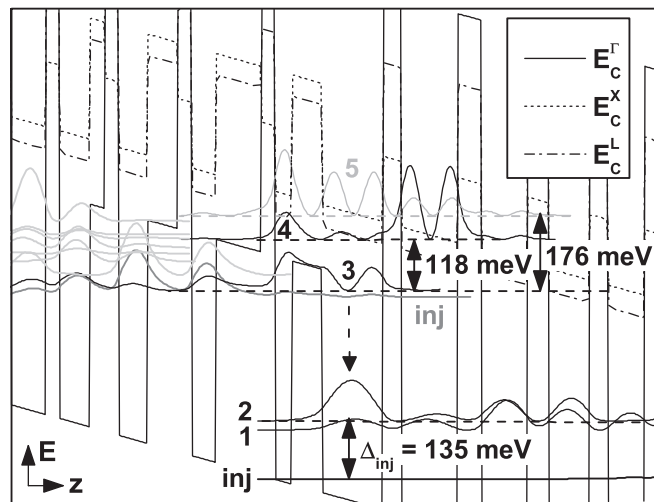


FIG. 2. A portion of the conduction band profile of the structure S1 under 100 kV/cm electric field. Layer composition and thickness are indicated in the original publication by Semtsiv *et al.*²⁰ Solid lines represent the moduli-squared of relevant Wannier-Stark states. The dashed arrow represents the lasing transition. Relevant states are labeled in analogy to Figure 1.

TABLE I. Energy differences of subband's minima for structures S1 and S2 (in meV) obtained following intersubband spacing calculations within the effective mass approximation. For a schematic representation of the energy levels, see Figures 2 and 3.

Structure	$E_3 - E_2$	$E_3 - E_{inj}$	$E_4 - E_3$	$E_5 - E_3$	Δ_{inj}
S1	300	14	118	176	135
S2	271	11	81	139	116

structure S2 ($4.6 \mu\text{m}$) larger in respect to the shorter-wavelength structure S1 ($3.9 \mu\text{m}$). Similarly, the probability for thermal backfilling $\propto \exp(-\Delta_{inj}/k_B T_e)$,⁶ i.e., the repopulation of the lower laser state 2 by carriers coming from the injector ground state, is in structure S2 by a factor of ~ 5 larger than in structure S1 ($\Delta_{inj}^{S1} = 135$ meV and $\Delta_{inj}^{S2} = 116$ meV). Although thermal backfilling is avoided designing injector regions with a large activation energy Δ_{inj} ,²⁻⁴ in general terms, this additional contribution would be included in the extracted thermal escape current density J_{esc} , reducing the injection efficiency η_{inj} into the upper laser level and increasing, in turn, the “lost” current density $(1 - \eta_3)J$.

Furthermore, reduced scattering of electrons from active region confined states into indirect valleys is expected due to the relatively high energies for indirect valley states. These energies can be estimated experimentally investigating the laser operation under the influence of a magnetic field, as shown by Semtsiv *et al.*²² Following this reference, the energy for indirect valley states lies about ~ 640 meV above the bottom of the $\text{In}_{0.73}\text{Ga}_{0.27}\text{As}$ Γ -valley. This value is comparable with confinement energies for excited miniband states lying above the Γ -valley excited state 5 (Figures 2 and 3), suggesting a minor contribution of intervalley carrier scattering to the total escape current.

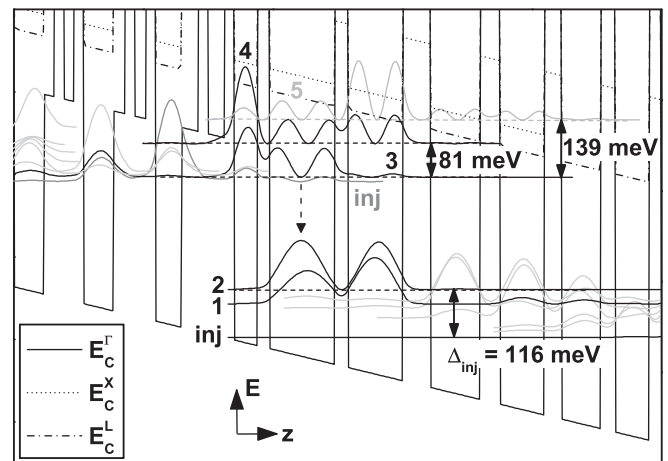


FIG. 3. Conduction band profile of the structure S2 under 76 kV/cm electric field. The layer thickness in nm from left to right starting from the widest active region quantum well are 5.0/1.0/4.2/2.1/3.8/1.5/3.4/1.3/3.0/1.1/2.6/0.9/2.3/0.8/0.7/0.8/0.7/2.3/0.9/0.7/0.9/0.7/2.0/1.3/0.7/1.3/0.7/1.8/0.9. AlAs layers are in bold, $\text{In}_{0.73}\text{Ga}_{0.27}\text{As}$ layers are in roman, and $\text{In}_{0.55}\text{Al}_{0.45}\text{As}$ layers are in italics. Underlined layers are doped to $1.5 \times 10^{18} \text{ cm}^{-3}$. Solid lines represent the moduli-squared of relevant Wannier-Stark states. The dashed arrow represents the lasing transition. Relevant states are labeled in analogy to Figure 1.

B. Reconstruction of the thermal escape current density at laser threshold

The mirror loss of our uncoated laser ridges is given by $\alpha_m = -\ln(R)/L$, where $R = [(n_{\text{eff}} - 1)/(n_{\text{eff}} + 1)]^2$ is the facet-reflectivity and L is the resonator length. The effective refractive index of the laser waveguide n_{eff} is determined from mode spacing measurements using a Fourier transform infrared spectrometer. At $T = 80$ K, a mode spacing of $\Delta\nu = 1.51 \pm 0.02 \text{ cm}^{-1}$ is measured for a $1.055 \text{ mm} \times 25 \mu\text{m}$ sample of structure S1 at laser threshold. The correspondent values for $n_{\text{eff}} = 3.14 \pm 0.04$ and $R = 0.26 \pm 0.01$ are extracted. At $T = 300$ K, no differences with the previous values were observed. Since the highest resolution of our spectrometer is 0.2 cm^{-1} , mode spacing variations due to small variations of the effective refractive index remain difficult to detect. As a matter of fact, variations of the refractive index in the infrared-range, and correspondingly of the facet-reflectivity, are expected to be of the order of 1%–2% in the temperature range of 80–300 K, as in the case of, e.g., GaAs.²³ Thus, for the further analysis, we assume an averaged value for the facet-reflectivity of $R = 0.26$ for both structures in the temperature range of this investigation.

Following Eq. (5), we expect a linear $1/L$ -dependence of J_{th} with different slope and y-axis-intercept values at different temperatures. Figure 4 illustrates this behavior based on measurements on samples of three different resonator lengths of structure S1. The modal gain coefficient $g\Gamma$ can be directly extracted from the slopes in Figure 4. Results are shown in Figure 5 for structures S1 and S2.

The calculated optical confinement of the main laser mode is $\Gamma = 0.77$ for the 40-stage structure S1 and $\Gamma = 0.60$ for the 30-stage structure S2. Hence, we obtain a gain coefficient ranging from $g = 14.0(9.3) \text{ cm/kA}$ at $T = 160$ K to $5.4(5.6) \text{ cm/kA}$ at room temperature for structure S1(S2). Similar results have been reported for $\lambda \approx 8 - 10 \mu\text{m}$ InGaAs/InAlAs QCLs²⁴ using the Hakki-Paoli technique.²⁵

The y-axis-intercept values at different temperatures in Figure 4 are $J_{th}(T, L \rightarrow \infty) = \alpha_w/(g\Gamma) + J_{th}^{esc}$. Multiplying

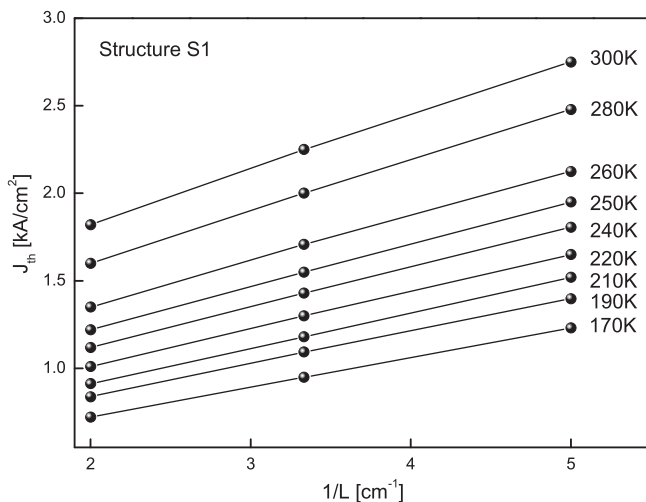


FIG. 4. Threshold current density as a function of reciprocal resonator length at different heat sink temperatures for structure S1. The solid lines illustrate the expected linear $1/L$ -dependence at different heat sink temperatures.

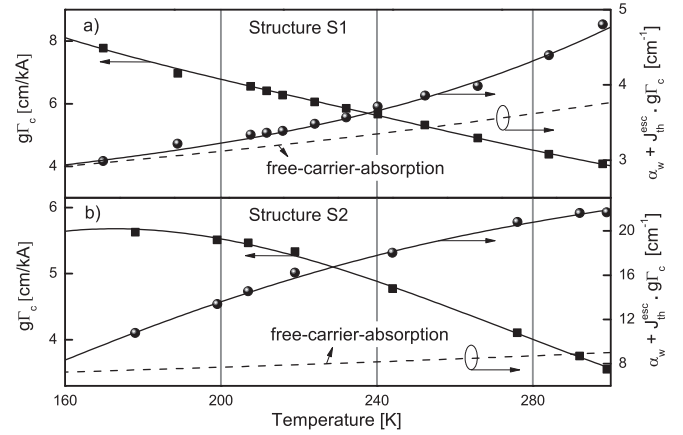


FIG. 5. (a) Modal gain coefficient $g\Gamma$ (solid squares) and $\alpha_w + J_{th}^{esc}(T) \cdot g\Gamma$ (solid dots) as a function of heat sink temperature for structures S1 (a) and S2 (b). The solid lines represent polynomial fits to the data. The calculated waveguide loss α_w due to free-carrier-absorption is also shown (dashed lines).

by the modal gain coefficient, we obtain $J_{th}(T, L \rightarrow \infty) \cdot (g\Gamma) = \alpha_w + J_{th}^{esc} \cdot (g\Gamma)$, which is plotted on the right axis in Figure 5.

Since the waveguide loss α_w in mid-IR QCLs is mainly determined by free-carrier absorption,²⁶ we calculate values for the free-carrier absorption coefficient in our QCL-structures (active region + cladding layers) and identify them with the waveguide loss. These are calculated using a semi-classical Drude free-electron model extended to doped semiconductors. Here, the semiconductor's dielectric function is written within a damped dielectric oscillator model including contributions from both optical phonons and free-carriers^{27,28} as

$$\epsilon(\omega) = \epsilon_{\infty} \left[1 + \frac{\omega_{LO}^2 - \omega_{TO}^2}{\omega_{TO}^2 - \omega(\omega + i\gamma_{ph})} - \frac{\omega_p^2}{\omega^2 + i\omega\gamma_c} \right], \quad (11)$$

where ϵ_{∞} is the high frequency dielectric constant, ω_{LO} and ω_{TO} are the longitudinal- and transverse optical phonon frequencies, respectively, γ_{ph} is the phonon damping constant, $\omega_p = [N_I e^2 / (\epsilon_0 \epsilon_{\infty} m_e^*)]^{1/2}$ is the plasma frequency of the free-carriers screened by the high frequency dielectric constant ϵ_{∞} , N_I is the free-carrier's concentration with effective mass m_e^* , e is the electronic charge, ϵ_0 is the vacuum permittivity, and the carrier's damping frequency $\gamma_c^{-1} = m_e^* \mu_e / e$ is given by the inverse of the relaxation time.

The free carrier absorption coefficient $\alpha_w = 4\pi\kappa/\lambda$ for radiation with free-space wavelength λ is determined by the imaginary part of the refractive index or extinction coefficient $\kappa = \text{Im}[\epsilon(\omega)]/(2n_r)$. Here, $\text{Im}[\epsilon(\omega)]$ is the imaginary part of the dielectric function and n_r is the real part of the refractive index. The phonons contribution to $\text{Im}[\epsilon(\omega)]$ is several orders of magnitude 10^{-2} – 10^{-1} smaller than the contribution of the free-carriers part, considering typical doping levels $N_I = 10^{17}$ – 10^{18} cm^{-3} and wavelengths $\lambda < 10 \mu\text{m}$ (material parameters can be found elsewhere in the literature, e.g., in Adachi's²⁹ work). On the other hand, $\omega \gg \gamma_c$ is fulfilled in our short-wavelength structures. Thus, ignoring the phonons contribution, we write $\text{Im}[\epsilon(\omega)] = \epsilon_{\infty} \gamma_c \omega_p^2 / \omega^3$ and the resulting free-carrier absorption coefficient as^{30,31}

$$\alpha_w(N_I, T, \lambda) = \frac{N_I e^3 \lambda^2}{4\pi^2 \epsilon_0 c^3 \mu_e(N_I, T) m_e^* n_r}. \quad (12)$$

The carrier's mobilities $\mu_e(N_I, T)$ are calculated using an extended version of the heuristic relation given by Caughey and Thomas³² to describe the temperature dependence of the charge carrier's mobility at low electric fields in Si. Generalizing this expression to III-V semiconductor compounds, the total mobility considering scattering on both LO-phonons and ionized impurities is written as

$$\mu_\nu(N_I, T) = \mu_\nu^{\min}(T) + \frac{\mu_\nu^L(T) - \mu_\nu^{\min}(T)}{1 + [N_I/N_\nu^{\text{ref}}(T)]^{1/\nu}}, \quad (13)$$

where $\nu = \{e, h\}$ indicate the charge carrier's type and N_I is the concentration of ionized impurities. In this model, the temperature dependence of the lattice mobility $\mu_\nu^L(T)$ and the ionized impurity contribution are parametrized with temperature and material dependent coefficients extracted from experimental data. This approach has been successfully applied into the modeling of a variety semiconductor materials and devices.^{33–36}

For both structures S1 and S2, the doping levels N_I in the injector and InP:Si cladding regions are taken to be n-doped to $1.5 \times 10^{18} \text{ cm}^{-3}$ and $1.5 \times 10^{17} \text{ cm}^{-3}$, respectively, and, an averaged value for the refractive index $n_r \approx n_{\text{eff}} = 3.14$, as calculated from mode spacing measurements, is considered. A useful summary of the additional material's parameters can be found in the works of Evans²⁷ and Palankovski.³⁶ With this approach, the waveguide loss is determined and also included in Figure 5. Furthermore, experimental studies have been done in order to determine the free-carrier absorption coefficient in doped III-V semiconductor compounds and, in particular, small values varying very little in the temperature range of 100–300 K have been reported for n-doped GaAs and InAs in the infrared region.^{37,38} Extracting data from these references, a free-carrier absorption coefficient within $2\text{--}4 \text{ cm}^{-1}$ is estimated in the temperature range of 100–300 K for wavelengths near $4.0 \mu\text{m}$. These values lie in the same order of magnitude with the calculated ones following Drude free-electron model calculations, as inspection of Figure 5(a) shows. Due to the increased portion of injector's doped layers and the larger emission wavelength in structure S2, the resulting values for the free-carrier absorption coefficient are for this structure ~ 2 -times larger than in structure S1 (Figure 5).

Finally, it is interesting to note that the found values for waveguide loss in the early mentioned work of Liu *et al.*²⁴ were 2-3-times larger than the estimated values for free-carrier absorption. Liu *et al.*²⁴ suggested that resonant-absorption mechanisms could be responsible for the excess on waveguide loss. On the other hand, the apparent excess on waveguide loss could arise from the neglected contribution of the leakage current at laser threshold J_{th}^{esc} .

With the previous considerations, and following Eq. (5), the thermal escape current density at laser threshold can be reconstructed as $J_{th}^{\text{esc}} = J_{th} - J_{th}^0$. These two components are shown in Figure 6, and the extracted values for J_{th}^{esc} can be

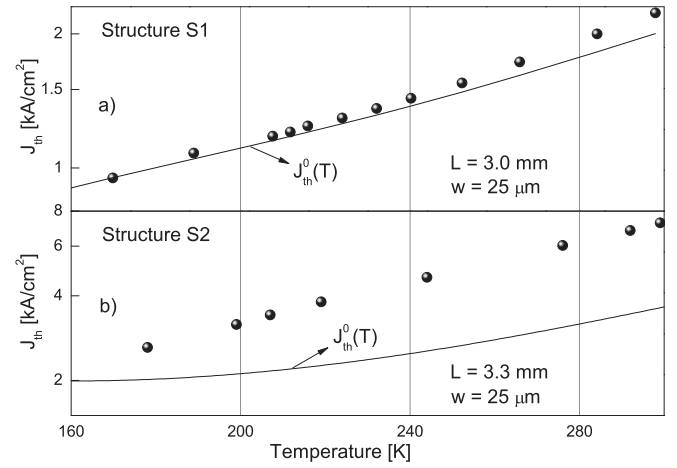


FIG. 6. Measured threshold current density (solid dots) for two samples of the studied QCL-structures as a function of heat sink temperature. The solid lines represents the expected threshold current density without the thermally activated leakage current.

found in Figure 7. Inspection of this figures shows, that in the case of structure S1, the thermal escape current density becomes significant at $T_c \approx 250 \text{ K}$ and its ratio to the threshold current density increases with temperature, reaching a value of $J_{th}^{\text{esc}}/J_{th} \approx 0.1$ at 300 K for the $25 \mu\text{m} \times 3.0 \text{ mm}$ sample (Figure 6(a)). A value of $J_{th}^{\text{esc}}/J_{th} \approx 0.15$ at 300 K has been estimated for conventional three quantum well QCL-structures.^{6,46} In the case of structure S2, the thermal escape current density achieves even higher values over the temperature scale (Figure 6(b)). A ratio of $J_{th}^{\text{esc}}/J_{th} \approx 0.5$ is reached at $T = 300 \text{ K}$ for a $25 \mu\text{m} \times 3.3 \text{ mm}$ sample of structure S2.

C. Determination of the activation energies

Assuming a nearly temperature independent averaged escape time τ_{esc} , we model the escape current density with Eq. (10) varying two independent fitting parameters, namely $C_1 = en_i/\tau_{\text{esc}}$ and E_{esc} . The variation of the LO-phonon

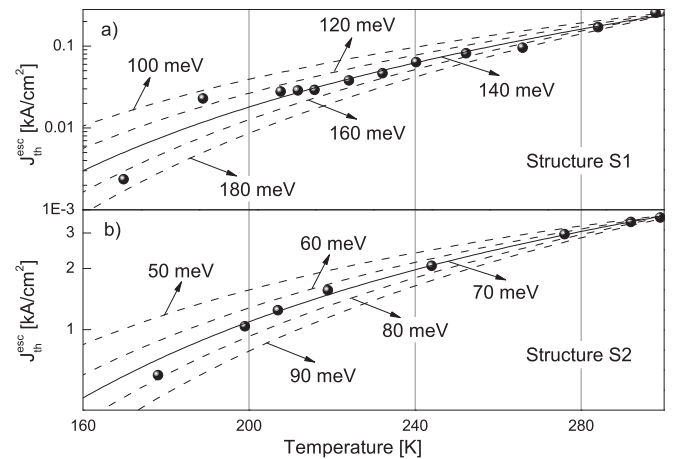


FIG. 7. Experimental values for the escape current density at laser threshold (solid dots) for structures S1 (a) and S2 (b) as a function of heat sink temperature. Fitting this current with Eq. (10), the experimental points can be reconstructed. The several lines represent best fits to the data for different activation energies $E_{\text{esc}} = 100, 120, 140$ (solid line), 160, and 180 meV, in the case of structure S1, and $E_{\text{esc}} = 50, 60, 70$ (solid line), 80, and 90 meV, for structure S2.

TABLE II. Fitting parameters for the determination of the thermal escape current density in the studied QCL-structures. The last column represents the averaged scattering time τ_{esc}/f_{ph}^{MB} calculated at $T_l = 300$ K assuming $E_{LO} \sim 32$ meV and a typical subband's concentration of charge carriers $n_i \sim 10^{10} \text{ cm}^{-2}$.

Structure	E_{esc} [meV]	C_1 [kA/cm ²]	τ_{esc}/f_{ph}^{MB} [ps]
S1	140 ± 20	24 ± 10	0.23 ± 0.1
S2	70 ± 5	27 ± 4	0.2 ± 0.05

energy is expected to be of the order of 1% in the temperature range of 80–300 K, as typical for III-V compound semiconductors.^{39,40} Thus, an averaged value $E_{LO} \approx 32$ meV is assumed for the studied temperature range. The subband's electronic temperature is determined from the lattice temperature and the injected current density using the phenomenological formula $T_e = T_l + \alpha_L \cdot J$.⁴¹ Here, T_l is the lattice temperature (assumed to be equal to the heat sink temperature), α_L is the electron-lattice coupling constant, and J is the total injected current density. An electron-lattice coupling constant $\alpha_L = 34.8 \text{ Kcm}^2/\text{kA}$ for InGaAs/InAlAs QCLs has been measured.⁴² Furthermore, we assume thermalized electron distributions and equal electronic temperatures for all subbands.^{5,11,14}

The best fits were selected comparing the resulting values for the escape current density with the extracted ones from the experimental data. Results are shown in Figure 7 with fitting parameters summarized in Table II.

For structure S1, the best fits to the data are obtained for activation energies within $E_{esc}^{S1} \approx 140 \pm 20$ meV. Fitting the data with values $E_{esc} < 120$ meV would lead to an overestimation of the escape current density J_{th}^{esc} and, as expected, lower values of J_{th}^{esc} than the measured are obtained for larger values of E_{esc} . In the case of structure S2, fitting the escape current density with Eq. (10) results in an activation energy of $E_{esc}^{S2} = 70 \pm 5$ meV. Relatively high fitting-confidence is obtained in this energy range (Figure 7).

Furthermore, following Sec. III and Eq. (8), a temperature-dependent averaged scattering time

$$\tau_{i4}(T_l) \approx en_i/[C_1 f_{ph}^{MB}(E_{LO}, T_l)] \quad (14)$$

can be determined from the fitting parameter C_1 . We assume for this purpose a typical value for the subband density of charge carriers $n_i \sim 10^{10} \text{ cm}^{-2}$.^{11,13,14} For structure S1, this results in an averaged scattering time of $\tau_{i4}^{S1} = 0.7 - 0.23$ ps in the studied temperature range of 160–300 K. The obtained values in the same temperature range for structure S2 are $\tau_{i4}^{S2} = 0.6 - 0.2$ ps. Sirtori and Teissier³ indicated a typical scattering time for the thermal escape of charge carriers to $\tau_{scatt} \sim 0.2$ ps.

An underestimation of the activation energies is expected when fitting the data assuming a smaller kinetic energy of charge carriers, e.g., in the case of equal electronic and lattice temperatures $T_e = T_l$. In the case of structure S1, no deviations from the found activation energies are found assuming equal electronic and lattice temperatures due to the relatively wide tolerance range of ± 20 meV. In general, the

error by determining the activation energies assuming equal electronic and lattice temperatures is of the order of $|E_{LO}(1 - T_e/T_l)| \sim 10$ meV, and it might become significant for devices operating at higher current densities. As a matter of fact, in the case of structure S2, fitting the data assuming equal electronic and lattice temperatures leads to a smaller activation energy $E_{esc}^{S2}|_{T_e=T_l} = 60 \pm 5$ meV.

D. Interpretation of the found activation energies

Inspection of Tables I and II reveals that the found activation energy $E_{esc}^{S1} \approx (E_{35} + E_{34})/2 = 147$ meV for structure S1 approximates an averaged value between E_{34} and E_{35} , if following the notations of Figure 2. This is interpreted as an indicator for the escape current to be consisting principally by thermally activated charge carriers scattering from the upper laser state 3 into states 4 and 5.

As a matter of fact, the interaction strength for LO-phonon scattering of two-dimensional charge carriers is directly related to the square of the *electron-phonon coupling function*.^{14–17} This quantity, also known as the *form factor* for the electron-(LO)-phonon interaction, is the exchange integral, in the direction of confinement, between the envelope functions of the initial and final charge carrier's states and the correspondent component of the phonon-induced potential. Assuming charge carrier's confinement in z -direction, the (unnormalized) electron-phonon coupling function for LO-phonon scattering can be written as¹⁴

$$G_{if}(q_z) = \int \psi_f^*(z) \exp(-iq_z z) \psi_i(z) dz, \quad (15)$$

where (i, f) represent the initial and final states with envelope functions ψ_{if} , q_z is the z -component of the LO-phonon's wave vector, and the factor $\exp(-iq_z z)$ arises from writing the phonon-induced potential $\phi = \sum_{\vec{q}} \beta(\vec{q}) \exp(-i\vec{q} \cdot \vec{r})$ as a superposition of orthogonal phonon modes modulated with normalization coefficients $\beta(\vec{q})$. For full details, see the works of Lundstrom¹⁶ and Harrison.¹⁴

Following this approach, form factors G_{if} for the studied QCL-structures are calculated. Using the notations of Figure 2, Figure 8(a) shows the calculated form factors squared $|G_{if}|^2$ for the cases $(i, j) = (3, 5)$ and $(i, j) = (3, 4)$ for structure S1. Inspection of this figure reveals that $|G_{35}(q_z)|^2 > |G_{34}(q_z)|^2$ for the large majority of LO-phonon's momentum q_z , indicating a larger interaction strength for the case $(i, j) = (3, 5)$. As a result, combined, significant contributions of thermally activated carriers from the upper laser state 3 into states 4 and 5 would be the principal constituents of the escape current J_{esc} . This is in turn reflected by the fact that the measured activation energy for this structure $E_{esc}^{S1} \approx (E_{35} + E_{34})/2$ approximates an averaged value for the subband's minima separations between these levels. Further calculations for the cases $(inj, 5)$ and $(inj, 4)$ reveal that the form factors squared are in this cases ~ 10 -times smaller than in the previous ones (Figure 8(c)), indicating a much weaker coupling between the injector ground state and higher states via LO-phonon absorption. A reduced contribution of thermally activated carriers from the

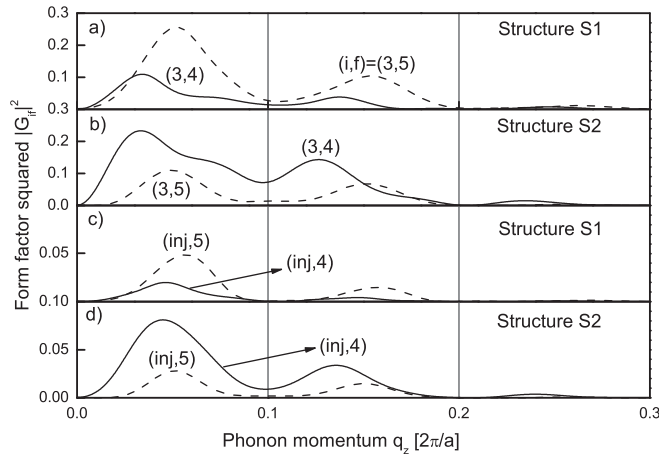


FIG. 8. Calculated form factors for the studied QCL-structures as a function of LO-phonon momentum in the direction of confinement. A mean lattice constant $a = 5.94 \text{ \AA}$ has been used for graphical representation purposes. The notations of Figures 2 and 3 are used for structure S1 (a), and S2 (b), respectively.

injector ground state to the escape current is expected due to the increased space overlap between this level and the upper laser state in 3-QW QCL-structures.¹⁰ As a consequence, the injection efficiency, η_{inj} in Eq. (3), is maximized, reducing the probability for scattering from the injector into higher states. Furthermore, an additional indicator for the reduced contribution of thermally activated charge carriers from the injector ground state to the total escape current are the found values for the fitting parameter C_1 . Indeed, if calculating the averaged scattering time τ_{i4} for the thermal activation process with Eq. (14) assuming a typical sheet density in the highly electron-concentrated injector ground state $n_{inj} \sim 10^{11} \text{ cm}^{-2}$,^{13,14} overestimated values by a factor of ~ 10 relative to the referred by the literature³ are found. (The previously assumed value $n_i \sim 10^{10} \text{ cm}^{-2}$ in Sec. IV C is a typical one for the sheet density in the upper laser level, as found from self-consistent rate equations calculations^{11,13,14}).

In the case of structure S2, the found activation energy $E_{esc}^{S2} \approx 70 \text{ meV}$ approximates the energy difference $E_4 - E_3 = 81 \text{ meV}$ between the upper laser level 3 and the next level with higher energy, labeled in Figure 3 as state 4. Again, as in the case of structure S1, weaker interaction strength is expected for LO-phonon absorption from the injector ground state, as form factor's calculations indicate (Figure 8(d)). However, in the case of structure S2, a reduced contribution of thermally activated carriers from the state 3 to 5 is expected, due to the reduced interaction strength for this case relative to structure S1 and to scattering into level 4 as well (Figure 8(b)). This, in turn, is reflected in the measured activation energy $E_{esc}^{S2} \approx E_{34}$ for this structure. Finally, as already mentioned in Secs. II and IV A, a lower activation energy E_{esc} than the expected one for thermal activation would be measured when additional leakage paths become more important. The small deviation of the measured activation energy from the expected value $E_{34}^{S2} - E_{esc}^{S2} \sim 10 \text{ meV}$ traces back to the increased contributions of additional scattering paths. Nevertheless, the fact that the found activation energies in both structures are close to the expected values

for thermal activation, suggests that the thermally activated scattering of charge carriers remains the dominant contribution to the “lost” current density $(1 - \eta_3)J$, as pointed out by Botez *et al.*⁶

Altogether, the found activation energies for the studied QCL-structures correspond well to the expected values for thermally activated leakage from the upper laser level 3. The thermal escape current consists then mainly from charge carriers within level 3 absorbing LO-phonons and scattering into higher states (Figures 2 and 3).

V. IMPACT OF THERMALLY ACTIVATED LEAKAGE ON QCL's TEMPERATURE-DEPENDENT CHARACTERISTICS

This section discusses the relation between the magnitude of the thermal escape current and the temperature-dependent performance and characteristics of the studied QCL-structures.

A. Summary of temperature-dependent characteristics of the studied QCL-structures

Figure 9(a) shows voltage-current and pulsed light output characteristics for a $25 \mu\text{m} \times 3.0 \text{ mm}$ device of structure S1. Tested laser ridges with uncoated facets were mounted epilayer up on Cu holders. The pulsed operated measurements were done with a pulse width of 300 ns and a duty cycle of 0.3%. The average optical power was measured using a thermopile detector placed directly in front of one laser facet, resulting in a collection efficiency of 100%. For temperature dependent measurements, the devices were mounted in a nitrogen gas flow cryostat. The heat sink temperature was measured using a Si-diode mounted close to the laser.

For structure S1, a threshold current density of 0.6 kA/cm^2 is measured at 80 K, which increases to 2.3 kA/cm^2 at 300 K. In this temperature range, the turn-on voltage U_{on} decreases from 23.6 V to 16.0 V, and the differential resistance remains nearly constant $dV/dI \approx 0.6 \Omega$.

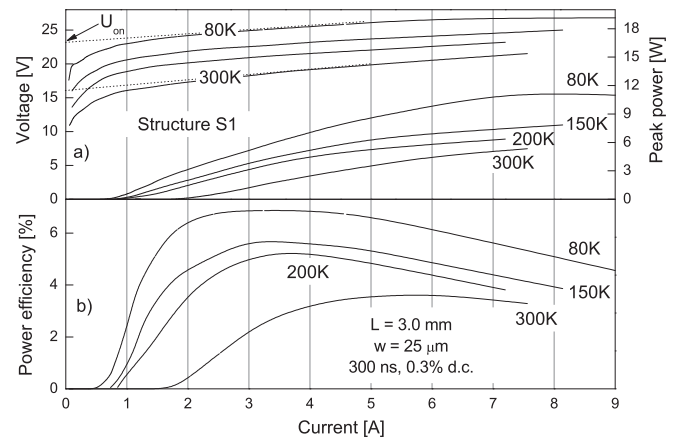


FIG. 9. Voltage-current and light-output (a) characteristics for a $25 \mu\text{m} \times 3.0 \text{ mm}$ sample of structure S1. Twice the single facet output is considered. The device was driven with 300 ns \times 10 kHz current pulses at different heat sink temperatures. The temperature dependence of the power efficiency is also shown (b).

A reduction of the turn-on voltage with increasing temperature is expected due to the broadening of the injector ground state subband's distribution. Furthermore, the relatively large increase of U_{on} at lower temperatures may be ascribed to the effect of the high strain compensation in our short-wavelength QCL-structures.⁴³ The differential slope efficiency dP/dI of 2.0 W/A (twice the single facet) at 80 K, correspondent to an external differential quantum efficiency η_{DQE} of 8.0 (0.2 per cascade), reduces at 300 K to 1.4 W/A, and 4.4 (0.1 per cascade), respectively. The emission wavelength is $\lambda = 3.9 \mu\text{m}$ at 300 K. The temperature dependence of the power efficiency $P/(UI)$ is shown in Figure 9(b). A maximal power efficiency of 6.9% is reached at 80 K, which decreases to 3.6% at 300 K.

Similarly, in the case of structure S2, a threshold current density of 1.86 kA/cm² is measured at liquid nitrogen temperatures for a $25 \mu\text{m} \times 3.3 \text{ mm}$ sample, increasing to 7.32 kA/cm² at room temperature. The output-power of this 30-cascade structure is relatively good, reaching peak powers of 4 W at 300 K. The external differential quantum efficiency per cascade of 0.26 at 80 K reduces to 0.1 at 300 K. The emission wavelength at room-temperature is $\lambda = 4.6 \mu\text{m}$.

B. Large activation energy and improved QCLs performance

Having a large activation energy, and, consequently, a reduced escape current, is advantageous for QCLs performance. The first, direct implication of this feature, is a high temperature insensitivity of J_{th} over temperature. The characteristic temperature T_0 is often introduced to parametrize J_{th} within a certain temperature range $[T_{min}, T_{max}]$. This parameter is defined in $J_{th}(T_{min} + \Delta T) = J_{th}(T_{min})\exp(\Delta T/T_0)$. High values of T_0 represent high temperature insensitivity and better QCLs performance. Furthermore, the value of T_0 is directly related to the maximal continuous-wave operating laser temperature.^{44,45} As shown in the left axis of Figure 10, a characteristic temperature of $T_0 = 175 \text{ K}$ is valid for

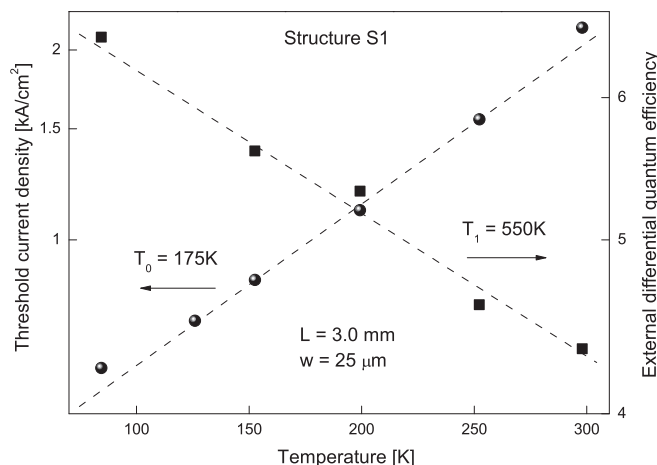


FIG. 10. Threshold current density (solid dots) and total external differential quantum efficiency (solid squares) as a function of heat sink temperature for the sample of Figure 9 (structure S1). The dashed lines represent exponential fits resulting in characteristic temperatures T_0 and T_1 as high as 175 K and 550 K, respectively, for this sample.

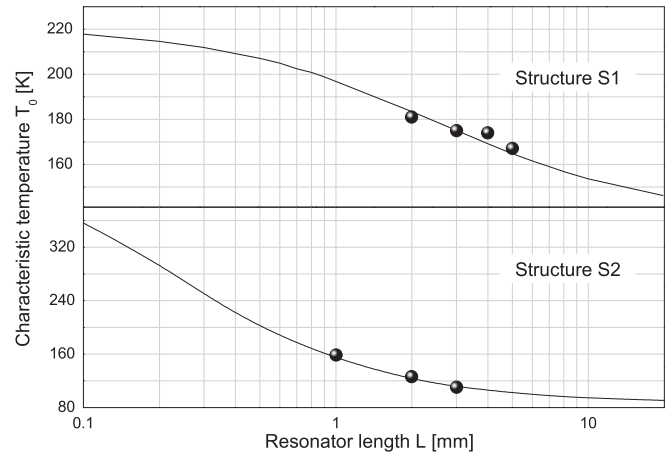


FIG. 11. Characteristic temperature T_0 as a function of the resonator length L for both structures studied in this paper. Expected values for T_0 (solid lines) can be extracted from a numerical analysis of the functional dependence of $J_{th}(T)$ on L . Experimental data are included as well (solid dots).

structure S1 in the temperature range of 150–250 K. This is a relatively good value and allows pulsed mode laser operation at room-temperature (Fig. 10).

A second, important consequence of a reduced escape current is the maximization of the upper laser state's lifetime. As a consequence, the transition efficiency η_{tr} , i.e., the probability for an electron in the upper laser level to undergo a radiative transition, is maximized as well. Furthermore, this quantity is directly related to the external differential quantum efficiency $\eta_{DQE} = (e/\hbar\omega)dP/dI = N_p\eta_{tr}\eta_{facet}$.^{2,12} Here, e is the electronic charge, \hbar is the Planck constant divided by 2π , ω is the central emission frequency, N_p is the number of cascades, and η_{facet} is the facet efficiency. Thus, increasing the lifetime in the upper laser state by reducing several leakage paths increases η_{DQE} as well. Analogous to the characteristic temperature T_0 , the phenomenological parameter T_1 is typically introduced to describe the temperature dependence of η_{DQE} within a temperature range $[T_{min}, T_{max}]$ as $\eta(T_{min} + \Delta T) = \eta(T_{min})\exp(-\Delta T/T_1)$. As the right axis of Figure 10 shows, a characteristic temperature $T_1 = 550 \text{ K}$ is extracted for structure S1, reflecting a high temperature insensitivity of η_{DQE} . This value is comparable with the bests reported for short-wavelength QCLs.⁹

An increased leakage current has considerable implications in the device's performance. Characteristic temperatures of $T_0 = 110 \text{ K}$ and $T_1 = 210 \text{ K}$ are valid in the temperature range of 150–250 K for a $25 \mu\text{m} \times 3.3 \text{ mm}$ sample of structure S2.

VI. VARIATION OF THE CHARACTERISTIC TEMPERATURE T_0 ON THE RESONATOR LENGTH

One additional, interesting consequence of knowing the factors that determine the behavior of the necessary current density to achieve laser threshold in a given temperature range is the capacity to estimate the dependence of the phenomenological parameter T_0 on the resonator length.

As already seen, the temperature dependence of the threshold current density varies with the resonator length L (Figure 4). Furthermore, a numerical analysis shows that the

functional dependence of $J_{th}(T)$ on L converges at very small (<0.1 mm) and large (>10 cm) resonator lengths. Therefore, a convergence character of T_0 at these limits is expected. In addition, for typical resonator lengths between 1 and 5 mm, the relative change of the characteristic temperature T_0 could be significant (16% for structure S1 and 33% for structure S2). This behavior depends, however, both on the used materials and on the particular QCL design. Numerical results for the dependence of the characteristic temperature T_0 on the resonator length are shown in Figure 11 for structures S1 and S2. Experimental points are included in this figure as well.

A similar behavior can be derived for the characteristic temperature T_1 . Nonetheless, the correlation with the experiment is not straightforward to illustrate due to the large inherent uncertainty involved in the determination of T_1 .

VII. SUMMARY

An accurate and straightforward extension of the 3-level threshold condition for QCLs to include thermally activated leakage of charge carriers from the upper laser state into higher states (4-level active region) was formulated. A method was proposed to determine the current component arising for thermal activation at laser threshold. This current was modeled taking both the temperature dependent subband-distribution of charge carriers and LO-phonon probability. This method was used to analyze and compare the thermally activated leakage of charge carriers in two short wavelength strain-compensated InGaAs/InAlAs QCL-structures. Thermally activated leakage was found to be the dominant contribution to the leakage current density in QCLs. Our approach offers a straightforward and accurate method to analyze and troubleshoot thermally activated leakage in new QCL-active region designs.

¹J. Faist, F. Capasso, D. L. Sivco, C. Sirtori, A. L. Hutchinson, and A. Y. Cho, *Science* **264**, 553 (1994).

²C. Gmachl, F. Capasso, D. L. Sivco, and A. Y. Cho, *Rep. Prog. Phys.* **64**, 1533 (2001).

³C. Sirtori and R. Teissier, contribution in *Intersubband Transitions in Quantum Structures* (McGraw-Hill, 2006).

⁴J. Faist, F. Capasso, D. L. Sivco, A. L. Hutchinson, C. Sirtori, and A. Y. Cho, *Infrared Phys. Technol.* **36**, 99 (1995).

⁵P. Harrison, *Appl. Phys. Lett.* **75**, 2800 (1999).

⁶D. Botez, S. Kumar, J. C. Shin, L. J. Mawst, I. Vurgaftman, and J. R. Meyer, *Appl. Phys. Lett.* **97**, 071101 (2010).

⁷P. Harrison and R. W. Kelsall, *Solid-State Electron.* **42**, 1449 (1998).

⁸C. Pflügl, L. Diehl, A. Lyakh, Q. J. Wang, R. Maulini, A. Tsekoun, C. Kumar N. Patel, X. Wang, and F. Capasso, *Opt. Express* **18**, 746 (2010).

⁹Y. Bai, N. Bandyopadhyay, S. Tsao, E. Selcuk, S. Slivken, and M. Razeghi, *Appl. Phys. Lett.* **97**, 251104 (2010).

¹⁰J. Faist, M. Beck, T. Aellen, and E. Gini, *Appl. Phys. Lett.* **78**, 147 (2001).

¹¹P. Harrison and R. W. Kelsall, *J. Appl. Phys.* **81**, 7135 (1997).

¹²J. Faist, *Appl. Phys. Lett.* **90**, 253512 (2007).

¹³K. Donovan, P. Harrison, and R. W. Kelsall, *J. Appl. Phys.* **89**, 3084 (2001).

¹⁴P. Harrison, *Quantum Wells, Wires and Dots*, 3rd ed. (Wiley, Chichester, 2009).

¹⁵R. Ferreira and G. Bastard, *Phys. Rev. B* **40**, 1074 (1989).

¹⁶M. Lundstrom, *Fundamentals of Carrier Transport* (Addison-Wesley, Reading, Wokingham, 1990).

¹⁷X. Gao, D. Botez, and I. Knezevic, *J. Appl. Phys.* **103**, 073101 (2008).

¹⁸H. C. Liu, A. G. Steele, M. Buchanan, and Z. R. Wasilewski, *J. Appl. Phys.* **73**, 2029 (1993).

¹⁹D. Botez, *Appl. Phys. Lett.* **98**, 216101 (2011).

²⁰M. P. Semtsiv, Y. Flores, M. Chashnikova, G. Monastyrskiy, and W. T. Masselink, *Appl. Phys. Lett.* **100**, 163502 (2012).

²¹J. B. Khurgin, Y. Dikmelik, P. Q. Liu, A. J. Hoffman, M. D. Escarra, K. J. Franz, and C. F. Gmachl, *Appl. Phys. Lett.* **94**, 091101 (2009).

²²M. P. Semtsiv, M. Wienold, S. Dressler, W. T. Masselink, G. Fedorov, and D. Smirnov, *Appl. Phys. Lett.* **93**, 071109 (2008).

²³J. S. Blakemore, *J. Appl. Phys.* **62**, 4528 (1987).

²⁴Z. Liu, C. F. Gmachl, L. Cheng, F. S. Choa, F. J. Towner, X. Wang, and J. Fan, contribution in ITQW07 (Leeds, 2007).

²⁵B. W. Hakki and T. L. Paoli, *J. Appl. Phys.* **46**, 1299 (1975).

²⁶C. Sirtori, P. Kruck, S. Barbieri, H. Page, J. Nagle, M. Beck, J. Faist, and U. Oesterle, *Appl. Phys. Lett.* **75**, 3911 (1999).

²⁷C. A. Evans, contribution in *Quantum Wells, Wires and Dots*, 3rd ed. (Wiley, Chichester, 2009).

²⁸P. Y. Yu and M. Cardona, *Fundamentals of Semiconductors*, 4th ed. (Springer, 2010).

²⁹S. Adachi, *Handbook on Physical Properties of Semiconductors* (Springer, USA, 2004), Vol. 2.

³⁰K. Seeger, *Semiconductor Physics* (Springer, Wien, 1973).

³¹K. A. Bulashevich, V. F. Mymrin, S. Yu Karpov, D. M. Demidov, and A. L. Ter-Martirosyan, *Semicond. Sci. Technol.* **22**, 502 (2007).

³²D. M. Caughey and R. E. Thomas, *Proc. IEEE* **55**, 2192 (1967).

³³S. Selberherr, W. Hänsch, M. Seavey, and J. Slotboom, *Solid-State Electron.* **33**, 1425 (1990).

³⁴T. T. Mnatsakanov, M. E. Levinshtein, L. I. Pomortseva, S. N. Yurkov, G. S. Simin, and M. A. Khan, *Solid-State Electron.* **47**, 111 (2003).

³⁵C. A. Evans, D. Indjin, Z. Ikonić, P. Harrison, *J. Comput. Electron.* **11**, 137 (2012).

³⁶V. Palankovski, Ph.D. dissertation, Technische Universität Wien, 2000.

³⁷R. M. Culpepper and J. R. Dixon, *J. Opt. Soc. Am.* **58**, 96 (1968).

³⁸W. G. Spitzer and J. M. Whelan, *Phys. Rev.* **114**, 59 (1959).

³⁹G. Irmer, M. Wenzel, and J. Monecke, *Phys. Status Solidi B* **195**, 85 (1996).

⁴⁰D. Schneider, C. Brink, G. Irmer, and P. Verma, *Physica B* **256–258**, 625–628 (1998).

⁴¹V. Spagnolo, M. Troccoli, G. Scamarcio, C. Becker, G. Glastre, and C. Sirtori, *Appl. Phys. Lett.* **78**, 1177 (2001).

⁴²M. S. Vitiello, T. Gresch, A. Lops, V. Spagnolo, G. Scamarcio, N. Hoyler, M. Giovannini, and J. Faist, *Appl. Phys. Lett.* **91**, 161111 (2007).

⁴³J. S. Yu, A. Evans, S. Slivken, S. R. Darvish, and M. Razeghi, *Appl. Phys. Lett.* **88**, 251118 (2006).

⁴⁴M. Beck, D. Hofstetter, T. Aellen, J. Faist, U. Oesterle, M. Illegems, E. Gini, and H. Melchior, *Science* **295**, 301 (2002).

⁴⁵J. Faist, F. Capasso, C. Sirtori, D. L. Sivco, A. L. Hutchinson, and A. Y. Cho, *Appl. Phys. Lett.* **67**, 3057 (1995).

⁴⁶D. Botez, J. Shin, J. Kirch, C. Chang, L. Mawst, and T. Earles, *IEEE J. Sel. Top. Quantum Electron.* **PP**, 99 (2013).